



City Research Online

City, University of London Institutional Repository

Citation: Zhai, H., Wu, Q., Xiong, K., Yoshikawa, N., Sun, T. & Grattan, K. T. V. (2019). Investigation of the Viscoelastic Effect on Optical- Fiber Sensing and Its Solution for 3D-Printed Sensor Packages. *Applied Optics*, 58(16), pp. 4306-4314. doi: 10.1364/ao.58.004306

This is the accepted version of the paper.

This version of the publication may differ from the final published version.

Permanent repository link: <https://openaccess.city.ac.uk/id/eprint/22199/>

Link to published version: <https://doi.org/10.1364/ao.58.004306>

Copyright: City Research Online aims to make research outputs of City, University of London available to a wider audience. Copyright and Moral Rights remain with the author(s) and/or copyright holders. URLs from City Research Online may be freely distributed and linked to.

Reuse: Copies of full items can be used for personal research or study, educational, or not-for-profit purposes without prior permission or charge. Provided that the authors, title and full bibliographic details are credited, a hyperlink and/or URL is given for the original metadata page and the content is not changed in any way.

City Research Online:

<http://openaccess.city.ac.uk/>

publications@city.ac.uk

Investigation of the Viscoelastic Effect on Optical-Fiber Sensing and Its Solution for 3D-Printed Sensor Packages

HONGZHOU ZHAI,¹ QI WU,^{2,1,*} KE XIONG¹, NOBUHIRO YOSHIKAWA², TONG SUN³,
KENNETH T. V. GRATTAN³

¹State Key Laboratory of Mechanics and Control of Mechanical Structures, Nanjing University of Aeronautics and Astronautics, Nanjing, 210016, China

²Institute of Industrial Science, the University of Tokyo, 4-6-1 Komaba, Meguro-ku, Tokyo 153-8505, Japan

³School of Mathematics, Computer Science and Engineering, City, University of London, EC1V 0HB, UK

*Corresponding author: wuqi@iis.u-tokyo.ac.jp

Received XX Month XXXX; revised XX Month, XXXX; accepted XX Month XXXX; posted XX Month XXXX (Doc. ID XXXXX); published XX Month XXXX

Viscoelasticity is an effect seen in a wide range of materials and it affects the reliability of static measurements made using Fiber Bragg Grating-based sensors, because either the target structure, the adhesive used, or the fiber itself could be viscoelastic. The effect of viscoelasticity on FBG-based sensing has been comprehensively researched through theoretical analysis and simulation using a finite-element approach and a further data processing method to reconstruct the graphical data has been developed. An integrated sensor package comprising of an FBG-based sensor in a polymer host and manufactured by using three-dimensional printing was investigated and examined through tensile testing to validate the approach. The application of the 3D-printed FBG-based sensor package, coupled to the data process method has been explored to monitor the height of a railway pantograph, a critical measurement requirement to monitor elongation, employing a method that can be used in the presence of electromagnetic interference. The results show that the effect of viscoelasticity can be effectively eliminated, and the graphical system response allows results that are sufficiently precise for field use to be generated. © 2019 Optical Society of America

<http://dx.doi.org/10.1364/AO.99.099999>

1. INTRODUCTION

In recent decades, Fiber Bragg Grating (FBG)-based sensors have been introduced and are now widely used as an alternative to conventional strain gages and thermocouples because of their advantageous characteristics such as high sensitivity, immunity to electromagnetic interference (EMI), small size and being lightweight. Taking advantage of this, they have been used in various industrial sectors, significantly to enhance sensing performance over the use of conventional methods [1,2]. However, FBG sensors do show shortcomings due to their limited elastic elongation and low fracture durability, as a result of which FBG-based sensors can neither measure large elongations nor withstand some tougher test environments. To address these issues, appropriate sensor packaging technology that integrates the FBG-based sensors into suitable host material structures has been introduced and researched. Typical host materials are metals [3] and concrete [4], for example.

Besides using conventional methods for such sensor installation, such as gluing the fiber in which the FBG is written on a structural

surface [5] or embedding into a structure itself [6-8], using three-dimensional (3D) printing technology offers a new and promising way to meet the critical integration requirements of better FBG-based sensors. 3D printing can be used precisely to stack the melted 3D filament, layer-by-layer, under the control of a computer to achieve the final structure. Thus, FBG-based sensors can be easily embedded into customized components that may have complex geometric shapes and thus designed to suit particular applications. Among the variety of materials that can be used in 3D-printing technology, polymers are widely accepted because they can melt and solidify quickly. However, its use also induces a side-effect which typically results in errors in testing and evaluation i.e. the results of such tests can vary over time due to viscoelasticity in the materials [9,10]. Arising from this inevitable effect, polymer structures (and not limited to 3D-printing) show a creep phenomenon under constant stress or stress relaxation under constant strain. Consequently, the measurand determined in this way from an integrated FBG-based sensor shows non-negligible errors and thus an improved performance.

The viscoelastic effect exists not only in the 3D-printing of suitably packaged FBG-based sensors, but also the problem is evident in polymer optical fiber (POF) and adhesive glued FBG sensors. When the strain measured by the sensor written into a POF is larger than 2%, the Bragg wavelength shift in the fiber becomes time-dependent [11], due to a noticeable viscoelastic effect. Similarly, surface-bonded FBGs using a high viscoelastic bonding layer also lead to a low measurement accuracy [12]. The issue becomes more significant in 3D-printed FBG sensing packages because of the large polymer volume used and the disadvantageous fiber-to-polymer ratio. Multiple reports of measurements using 3D-printed sensing packages can be seen with a linearity elastic range in which the Bragg wavelength shift is quasi-linearly related to the strain [8,10]. These reports regularly do not fully explore the potential of measurements of larger strains by using 3D-printed sensing packages. Therefore, finding a way to solve the problem of errors created in such measurements due to viscoelastic effects that are seen to limit the precision of the result of applying the sensor is of real importance for the industrial community depending on the reliability of such measurements.

In this work, this problem is tackled and a comprehensive investigation of the viscoelastic effect on an optical fiber sensor mounted in a 3D-printed sensing package was undertaken. Here, Section 2 introduces the appropriate underpinning theory for 3 common conditions of the viscoelastic effect of FBG-based sensors. In Sections 3 and 4, a special dumbbell-shaped 3D-printed FBG-based packaged sensor is employed to validate the existence and nature of the viscoelastic effect with finite-element analysis and a tensile test, respectively carried out. In Section 5, a curve reconstruction approach, based on deconvolution is proposed and validated to allow a more effective interpretation of the core measurement data, which is not evident from the raw data. To validate this in an application which is important for industry, this sensing technique and the data processing algorithm are applied to displacement measurements made on a railway pantograph, to allow real-time height monitoring, as discussed in Section 6.

2. Theoretical Background

A. Linear Viscoelasticity

Viscoelasticity is a mechanical phenomenon in which the material properties are known to vary with time and temperature. The reasonable assumption is made that the mechanical properties of the polymer are temperature-independent because the service temperature of the sensing package is usually much lower than its glass transition temperature [13]. In addition, the linear viscoelasticity exhibited by polymers when the deformation is relatively small or in the early stages of large deformation is sufficiently precise to allow the mechanical responses of the POF [9,11], the adhesive [12] and the host material integrated with the FBG [10]. According to the Boltzmann superposition principle [14], the smooth strain history varies over time, which can be expressed through a definition of the integral,

$$\sigma(t) = \int_0^t E(t-\tau) d\varepsilon(\tau) \quad (1)$$

Eq. 1 can also be written in a form of the Stieltjes convolution:

$$\sigma(t) = E(t) * d\varepsilon(t) \quad (2)$$

For linear viscoelasticity, the generalized Maxwell model is a useful mean to illustrate the general principle of its response to small or slow deformation, that also can be converted into a generalized Kelvin-Voigt model according to the different topologic connection of a spring-

dashpot element[15]. The generalized Maxwell model consists of the sum of exponentials, shown as

$$E(t) = E_\infty + \sum_{j=1}^n E_j e^{-\frac{t}{T_j}} \quad (3)$$

Based on the discrete results obtained from a relaxation experiment, the constant of each element in Eq. 3 can be calculated by the use of the least-squares-curve-fitting method [16,17].

TABLE 1. NOMENCLATURE

Symbol	Parameters
Σ	Stress
E	Strain
E	Material moduli
G	Shear moduli of the material
J	Shear creep compliance of the material
T	Time
T	Relaxation time.
R	The Outer radial coordinate of the model
X	The longitudinal coordinate of the model
D	The width of the bonded FBG
H	The thickness of the adhesive interlayer
L	Length of the bonded FBG
γ	Effective relaxation modulus
$\xi, \tilde{\lambda}$	Eigenvalues utilized in Laplace domain

Subscripts c, p, a, h represent fiber, coating, adhesive and host layer, respectively. Subscript ∞ represents the long-term modulus, and the subscript i, n represents the element number and the total number of the spring-dashpot element, respectively.

B. Viscoelastic Effect on POF

The viscoelasticity in the POF is simple and straightforward because the whole sensing material that is the POF itself is isotropic and uniform. Large [11] has researched viscoelasticity in POFs using experimental methods. Through a strain-recovery test and a stress relaxation test, the stress relaxation and the strain creep of the POF was investigated, which, significantly, proved the existence of sensing errors induced by viscoelasticity, in polymer-based optical fiber sensors.

C. Viscoelastic effect on surface-boned FBGs

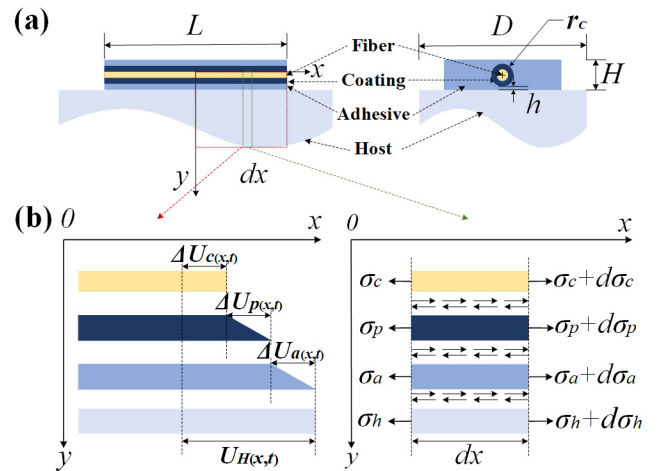


Fig. 1. Diagram of surface-bonded FBG: (a) schematic diagram and cross-section diagram, (b) displacement and stress analysis diagram.

The phenomenon becomes more complex when gluing a conventional silicon fiber onto an elastic host, as shown schematically in Fig. 1. The fiber and the host in this model are elastic, while the adhesive is linear viscoelastic. When the host is subjected to axial stress and undergoes a uniform strain, the fiber and adhesive are subjected to shear stress because they are glued tightly, that is without there being any slip between their interfaces. Using two reasonable assumptions that the strain gradients on the FBG and the bonding adhesive are of the same magnitude and the strain at the ends of the fiber and at the adhesive layer each are zero [12,18], the strain-transference function of the surface-bonded FBG sensors in the Laplace domain can be presented as follows:

$$\tilde{\varepsilon}_c(x, s) = \left[1 - \frac{\cosh(\tilde{\xi}x)}{\cosh(\tilde{\xi}L/2)} \right] \cdot \tilde{\varepsilon}_h(x, s) \quad (4a)$$

$$\frac{1}{\tilde{\xi}^2} = s \cdot \tilde{J}_a(s) \cdot \frac{(2\pi r_p + D)r_p E_c h}{4D} + \frac{(r_p + r_c)r_p E_c}{4G_p} \quad (4b)$$

where $\tilde{\varepsilon}_c(x, s)$, $\tilde{\varepsilon}_h(x, s)$ represents the Laplace transformed strain on the optical fiber and the host material, respectively. In formula 4(b), the constant $\tilde{\xi}$ is a function dependent on the creep compliance and geometric factor of each layer. Due to the viscoelastic function of the adhesive, $\tilde{J}_a(s)$ that is transformed from $J_a(t)$ represents the shear creep compliance in the Laplace domain. Thus, the strain on the FBG along the axial direction can be obtained by using the inverse Laplace transform.

$$\varepsilon_c(x, t) = \mathcal{L}^{-1} \left[1 - \frac{\cosh(\tilde{\xi}x)}{\cosh(\tilde{\xi}L/2)} \right] * \varepsilon_h(x, t) \quad (5)$$

where \mathcal{L}^{-1} represents the inverse Laplace transform.

D. Viscoelastic effect on the sensing packages

Another widely existing condition is that where the polymer package is integrated with the FBG sensor. Fig. 2 depicts a simplified cylinder model of an FBG embedded into a viscoelastic package. Based on previous research [10,18], the strain-transferring function of the embedded FBG in the Laplace domain can be presented as

$$\tilde{\varepsilon}_c(x, s) = \tilde{\varepsilon}_h(0, s) \cdot \left[1 - \frac{\sinh(\tilde{\lambda}x)}{\sinh(\tilde{\lambda}L/2)} \right] \quad (6a)$$

$$\tilde{\lambda}^2 = \frac{2\tilde{J}_c(s)}{r_c^2 \left[\tilde{J}_a(s) \ln \frac{r_a}{r_p} + \tilde{J}_p(s) \ln \frac{r_p}{r_c} \right]} \quad (6b)$$

Similarly, $\tilde{\varepsilon}_c(x, s)$ and $\tilde{\varepsilon}_h(0, s)$ respectively represent the strain on the FBG sensor and the middle point strain in the host. Besides, $\tilde{\lambda}$ is an eigenvalue dependent on both geometrical factors and material parameters. The strain on the FBG along the axial direction can be expressed in the time domain as

$$\varepsilon_c(x, t) = \mathcal{L}^{-1} \left[1 - \frac{\sinh(\tilde{\lambda}x)}{\sinh(\tilde{\lambda}L/2)} \right] * \varepsilon_h(0, t) \quad (7)$$

The strain transference functions of the embedded and surface-bonded FBGs, i.e., Eq. 7 and 5, are different, this mainly being caused by the different assumptions and boundary conditions utilized in the models [18]. However, the strain on the fibers always is expressed by a

convolution of the strain on the packaging material and a strain transfer coefficient.

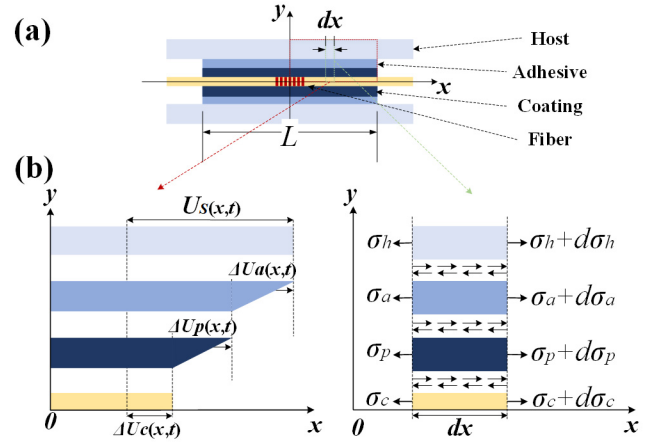


Fig. 2. Concentric cylinder model of 3D-printing FBG sensing package: (a) schematic diagram along axial direction, (c) displacement and stress analysis diagram.

E. Discussion of viscoelastic effect

To clearly analyze the viscoelastic effect in the FBG-integrated sensors, an analytical discussion on the bonded FBG sensor is discussed in detail. When a step load is subjected to the bonded FBG sensing system, the host strain in Eq. 5 can be expressed as

$$\varepsilon_h(x, t) = \varepsilon_h(x) \cdot H(t) \quad (8)$$

where $H(t)$ is a step function,

$$H(t) = \begin{cases} 1 & t \geq 0 \\ 0 & t < 0 \end{cases} \quad (9)$$

Eq. 10 is the Laplace-domain expression of Eq. 8:

$$\tilde{\varepsilon}_h(x, s) = \frac{\varepsilon_h(x)}{s} \quad (10)$$

Then, the transferred strain can be presented as

$$\varepsilon_c(x, t) = \varepsilon_h(x) \cdot \mathcal{L}^{-1} \left\{ \frac{1}{s} \left[1 - \frac{\cosh(\tilde{\lambda}x)}{\cosh(\tilde{\lambda}L/2)} \right] \right\} \quad (11)$$

$\gamma(x, t)$, defined as the creep transfer coefficient, can be written as

$$\gamma(x, t) = \frac{\varepsilon_c(x, t)}{\varepsilon_h(x)} = \mathcal{L}^{-1} \left\{ \frac{1}{s} \left[1 - \frac{\cosh(\tilde{\lambda}x)}{\cosh(\tilde{\lambda}L/2)} \right] \right\} \quad (12)$$

Since the right-hand part of the Eq. 12 is hard to solve with the inverse Laplace transform, the exponential function (Eq. 13) associated with a least-squares-curve-fitting method was employed to calculate the strain transfer coefficient in the time domain.

$$y = a + b \cdot e^{-\frac{t}{\tau}} \quad (13)$$

Fig. 3 depicts the variation of the strain transfer coefficients versus longitudinal coordinates at a different time, that is calculated with the parameter listed in Table 2. Curves with different colors represent the strain transfer coefficient at 0, 100, 200, 300, 400, and 500 s, illustrating the decrease of the strain transfer coefficient because of the viscoelasticity of the adhesive. Although the position near to the center part has a relatively uniform strain transfer coefficient, it varies significantly near to the ends of the bonding part, which is the well-known shear-lag effect [19,20]. In actual applications, the FBG usually

locates near to the center, leading to Bragg wavelength shifts under a uniform strain, rather than to allow spectrum distortion. The Bragg wavelength shift can be related approximately to the average strain transfer coefficient.

TABLE 2. Values of Each Parameter used

Symbol	Values	Units
E_c	72	GPa
G_p	0.4	GPa
G_{a1}	1.1429	GPa
G_{a2}	0.02	GPa
η_2	58.82	GPa·s
L	20	Mm
r_c	62.5	Um
r_p	125	Um
r_a	250	Um

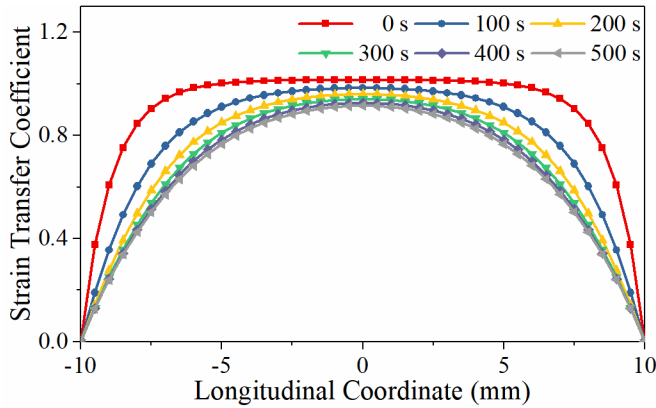


Fig. 3. The strain transfer coefficient of bonded FBG.

Moreover, because Eq. 5 and 7 are efficient ways to predict the strain transfer from the host material to the FBG, albeit with a different format, a consistent expression for the transferred strain can be given in the Stieltjes convolution form:

$$\varepsilon_c(x, t) = Y(x, t) * \varepsilon_h(x, t) \quad (14)$$

where $Y(x, t)$ represents the effective relaxation modulus, which depends on the viscoelastic modulus and the geometrical factors of the polymer and adhesive that utilized during the setting of the FBG. Although $Y(x, t)$ can be directly calculated if the viscoelasticity of the polymer material and the geometric information on the packaged structure is known, its value obtained from this idealized method is influenced by the resolution of the 3D printer and the extent of the manufacturing error that occurs. Another efficient method for obtaining the effective viscoelastic modulus by using the stress relaxation test is introduced in Sections 5 and 6.

3. Finite Element Analysis

For further exploring the viscoelastic effect on the FBG integrated 3D-printing sensing component, a finite-element analysis of the uniaxial tensile test was executed using ABAQUS. A 3D model of the dumbbell specimen test was created according to ISO 527-1&2. In the model, an embedded FBG was simplified to be represented as a column with a length of 20 mm and a diameter of 250 μm . The dimensions of the model are depicted in Fig. 4(a), and an encastre boundary condition was applied to the left-hand end, whereas a step function displacement was applied to the right-hand end. The whole

model was meshed into 41736 hybrid 3D continuum elements (C3D8H). Then, a “visco” step (special analysis step setting for viscoelasticity in ABAQUS) was created for the one-dimensional tension test of the polymer.

The packaging material was a thermoplastic polyurethane (TPU), and its viscoelastic modulus was obtained by using an experimental measurement method introduced later (in Section 4.3). A control model assuming that the TPU is purely elastic was also investigated. The optical fiber had a Young’s modulus of 72 GPa and a Poisson’s ratio of 0.21 [4,21].

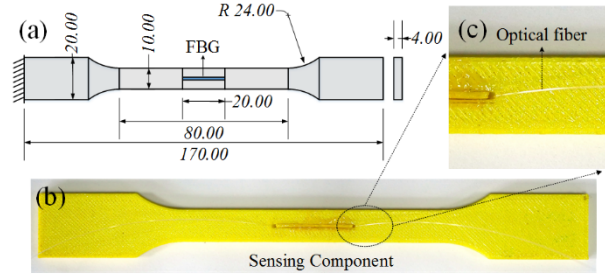


Fig. 4. Geometric model of the specimen: (a) geometry of the dumbbell specimen, (b) dumbbell sensing component integrated with the FBG, and (c) enlarged view of the 3D-printing sensing specimen showing the embedded optical fiber sensor.

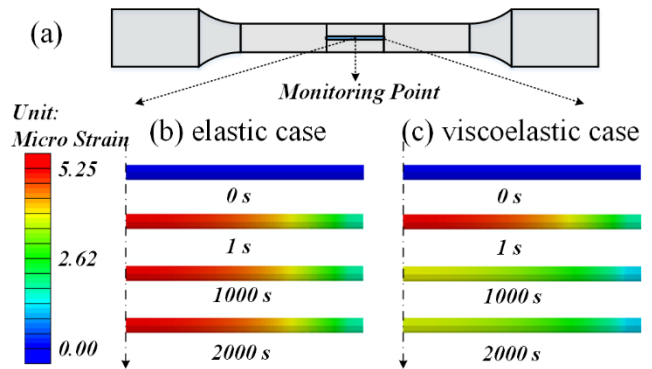


Fig. 5. Strain contours on FBG: (a) geometry model, (b) strain contours of the elastic case, and (c) strain contours of the viscoelastic case.

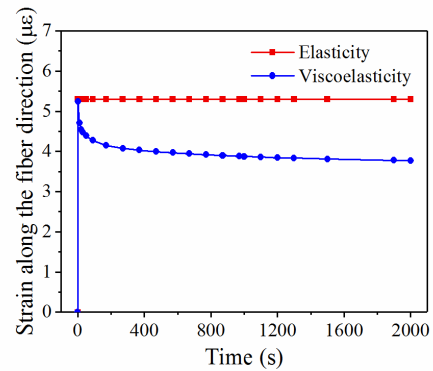


Fig. 6. Strain variation along the fiber direction.

Figure 5 shows the results of the simulation. Figure 5(b) and (c) show a comparison of the elastic and viscoelastic phenomena on the

right-half of the FBG. At the beginning of the experiment, the strain along the fiber direction was almost the same, because the stress within the polymer exhibited a barely visible relaxation phenomenon in a short time. Then, unlike the constant stress situation applied to the FBG shown in Fig. 5(b), the stress applied to the FBG decreased over time because of the relaxation of the polymer package that induced strain fading on the FBG, as shown in Fig. 5(c). One element in the center of the FBG was selected as the monitoring point to study the strain variation (the Bragg wavelength shift) on the FBG, as shown in Fig. 5(a). The strain curves on the FBG embedded in the elastic and viscoelastic hosts are shown in Fig. 6, these corresponding to the contour of the strain. Results from a Finite Element Analysis underpin the theoretical explanation of the viscoelastic effect, given in Section 2 and provided an impetus for the following experiments, described below.

4. Experiments

A. Fabrication of the test specimen

A model with the same geometric shape as was shown in Section 3 was input as the 3D printing fabrication program. The printer (J.H. Tech. Electronic Ltd.; Qubea QD-1) has a nozzle diameter of 0.4 mm, a speed of 2000 mm/min, and uses TPU resin. After the host was fabricated, the FBG sensor (Optounion tech. Ltd.; SMF-28, Bragg wavelength: 1550 nm; FBG length: 10 mm.) was integrated into the center groove of the host with an epoxy adhesive (EPO-TEC, ND353). A 3D printed cap was plugged into the groove, which roughly ensures the amount of adhesive used is consistent at any one time. The adhesive is cured at room temperature for 3 days. Two sensing packages were fabricated for the validation experiments. Fig 4(b) shows a photograph of a typical FBG sensing package, and Fig 4(c) shows the details of the embedded optical fiber sensor.

B. Tensile test

Fig. 7 shows a schematic diagram of the platform created for the tensile test. A tensile machine (Suns Test Tech. Co. Ltd., UTM5000) was used to create the displacement load. The 3D-printed sensing package embedded with the FBG sensor experienced a step function elongation (0.8 mm) for the relaxation test. A desktop computer with a sampling frequency of 15 Hz recorded the applied load, including the displacement and the force, on the tensile machine. An FBG interrogator (Micron Optics, Si425) with a sampling frequency of 250 Hz, and <0.2-pm resolution, recorded the Bragg wavelength shift.

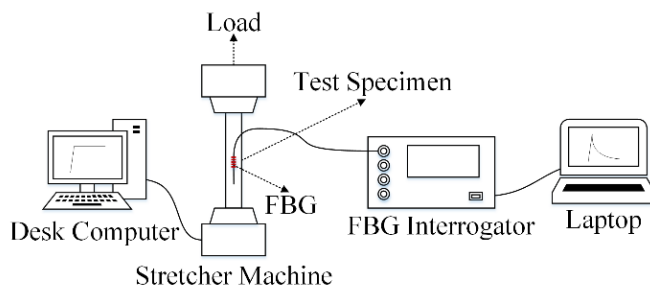


Fig. 7. Schematic diagram of the test platform.

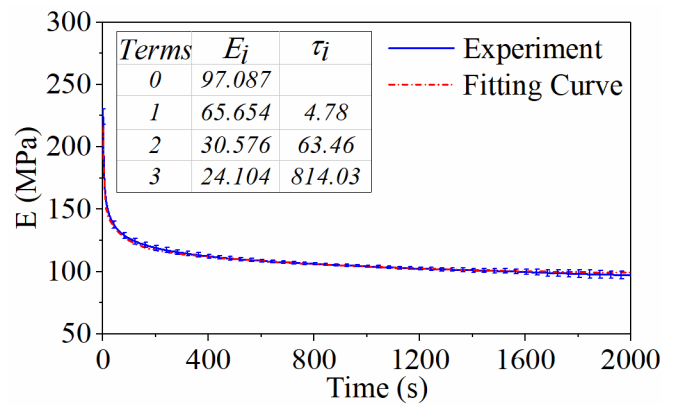


Fig. 8. Tensile results and Prony series fitting curve.

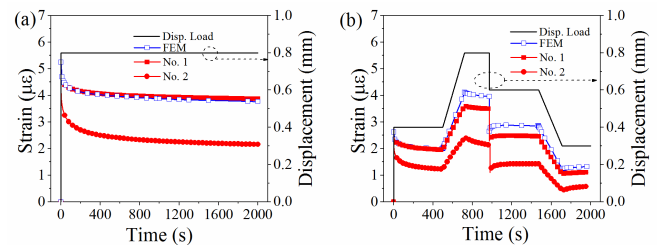


Fig. 9. The viscoelastic effect seen in the experiments carried out.

C. Viscoelastic of TPU

As shown in Fig. 8, the experimental results were pictured using a blue line. The red line is a graph of the four terms Prony series of viscoelasticity calculated with a least-square curve fitting method. Its Young's modulus is large initially, then it quickly decreases. After approximately 100 s, the rate of strain fading slows down. The stress fading is a typical characteristic of the viscoelasticity of the polymer package. The table in the figure shows the coefficient of the Prony series of the TPU.

D. Viscoelastic effect test

During their service life, sensors may suffer loads with different profiles so that it is necessary to study the viscoelastic effect under a complex loading condition that contains a combination of step loading, quasi-static loading, step unloading, and quasi-static unloading processes. In the experiment, a 0.4 mm displacement was first applied to the sensing package in 5 s, to approximate a step load, followed by another 0.4 mm displacement over the period from 500 s to 750 s to form a quasi-static load. Then, a 0.2 mm and 0.3 mm unloading process was applied on the sensing package at times 5 s and 250 s to approximate the stepped and quasi-static unloading process. The complex loading profile is representative of practical situations and an effective means to study the viscoelastic effect because other different loading profiles can be represented approximately by combining these four loading types. Two specimens were tested under both step loading and complex loading, and the experimental results obtained are depicted in Fig. 9(a) and (b). The black lines are the loading profiles applied to the dumbbell specimens, the blue lines are the FEM results, and the red lines are uniaxial tensile test results of two specimens. Compared with the results of Specimen 2, the relaxation curve of Specimen 1 fits the FEM result well. The difference between these two specimens is likely caused by the different fabrication and the gluing conditions, i.e., their effective viscoelastic moduli are different. In both the step loading and the complex loading considered, the experimental

results demonstrate the presence of the viscoelastic effect in these 3D-printing sensing specimens fabricated.

5. Reconstruction Methodology

A. Algorithm

Since the relationship between the Bragg wavelength shift and the overall elongation can be expressed in the form of the Stieltjes convolution, the overall elongation conversely can be obtained from a knowledge of the Bragg wavelength shift and the effective relaxation modulus, by using a newly proposed deconvolution method.

The reconstruction process for solving the viscoelastic influence is depicted in Fig. 10. Before its application, an effective relaxation modulus needs to be calibrated by using a uniaxial stress relaxation test. According to Eq. 14 and $\varepsilon = \Delta L/L$, when the overall elongation $\Delta L(t)$ is a stepped load, $d\Delta L(t)$ will be a Dirac delta function; thus, the strain curve measured from FBG, $\varepsilon_f(t)$ becomes proportional to the effective relaxation modulus, and the effective relaxation modulus $Y(t)$ can, therefore, be calculated. Because $Y(t)$ is influenced by the geometry and the gluing conditions in a practical application, it is recommended to obtain its value using the experimental method rather than accepting an analytical solution or results from a simulation using the finite element method.

After the calibration, a practical measuring test having a complex loading profile $\Delta L(t)$ is conducted. In this process, the strain on the FBG $\bar{\varepsilon}_f(t)$ can be measured. $Y(t)$ is used in a deconvolution process responding to Eq. 14, combined with $\bar{\varepsilon}_f(t)$ in the measurement test.

Therefore, the differential of displacement load $d\Delta\bar{L}(t)$ can be calculated. The last step of the reconstruction process is the integral of the results from the latest step, so that the reconstructed overall displacement load $\Delta\bar{L}(t)$ can, therefore, be obtained.

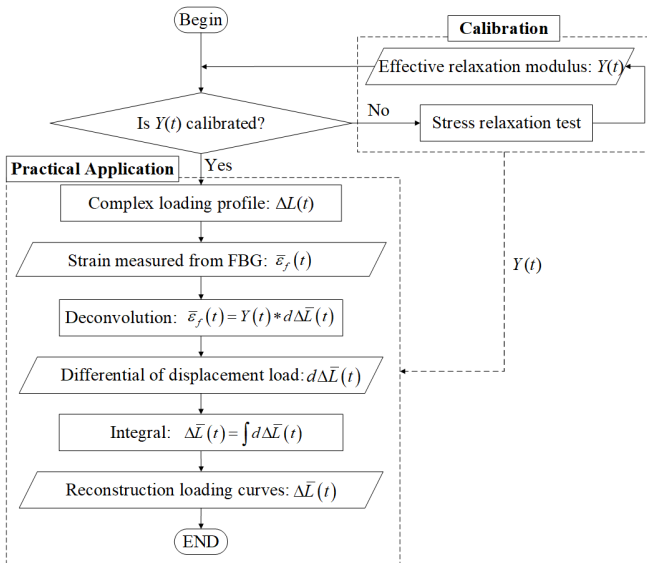


Fig. 10. Schematic of the reconstruction process.

B. Reconstruction performance

Fig. 11 shows the experimental displacement loads (black line), the experimental results of the strains on the FBGs (red lines with square marks), and the reconstruction graphs of the displacement loads (blue lines with circle dots) created through the reconstruction algorithm. Figs. 11(a) and (b) are the results of undertaking the uniaxial relaxation tests on Specimens 1 and 2, under step function loads. Because the effective viscoelastic modulus utilized for the deconvolution is from the test results, the reconstruction results correspond to the loading graphs very well. Figs. 11(c) and (d) depict the reconstruction results from Specimens 1 and 2, under a complex loading profile. The reconstruction graphs agree well with the loading graphs, which proves the accuracy and effectiveness of the reconstruction algorithm.

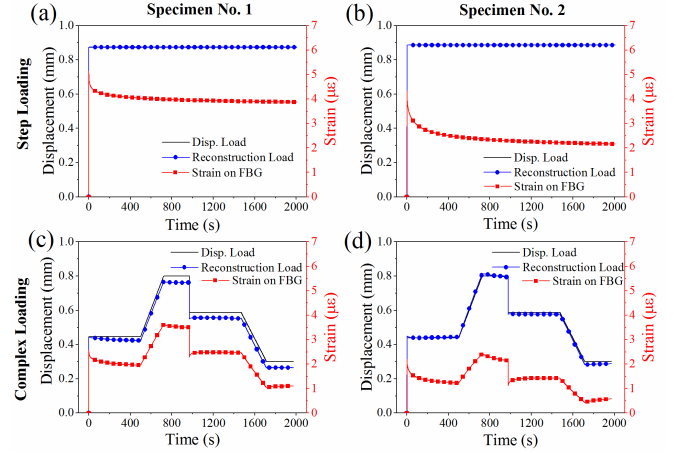


Fig. 11. Comparison of reconstruction results for specimens 1 and 2.

6. Application of the 3D FBG Package to Pantograph Height Monitoring

A. 3D FBG package mounted on the pantograph

A pantograph is an apparatus mounted on the roof of an electric train to collect power. By pushing a contact against the underside of the electric wire, the train can draw the electric power it needs to run. However, the contact between the pantograph and the electric wire is not always stable under operational conditions, because the train frequently encounters complex traffic conditions and different types of harsh environments. Unfortunately, the important information needed on the height of the pantograph cannot readily be measured, as conventional sensors are affected by electromagnetic interference (EMI) due to the environment. Therefore, sensors for height monitoring, with resistance to EMI, are of real importance to ensure the continuity of the operation and the safety of the train. This provides an illustrative example of the use of the approach to make an important industrial measurement.

Fig. 12(a) shows several typical 3D-printed sensing packages, which allow the integration of the FBG sensors. The manufacturing process was the same as that introduced in Section 4.A. The grooves shown in the components were used for embedding the sensing FBGs where, for example, the geometry of the third design makes it analogous to a spring. A relatively large elongation is possible but limited by the elastic strain limit of the silica optical fiber (that is 1-3%) [22]. The sensing device was installed on the joint of the pantograph, as shown in Fig. 12(b). Fig. 12(c) then shows that the joint can be rotated as the arm of the pantograph is lifted. As a result, the sensor itself is stretched and the height of the pantograph can be determined from a measurement

of the Bragg wavelength shift. Because of the thermoplastic materials used in the 3D-printed sensors, its optical nature allows it to have a high resistance to EMI. Its physical nature means it can also readily fit the geometric shape coming from the joint rotation. However, owing to the large viscoelasticity of this sensor, the raw data of the Bragg wavelength shift cannot simply be used to monitor the pantograph height, which is discussed below.

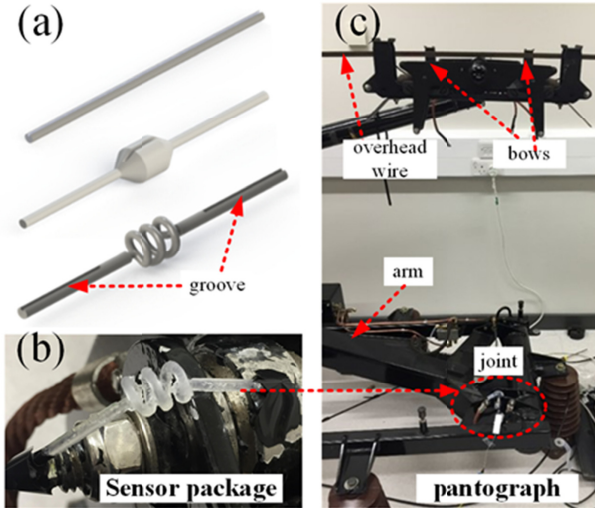


Fig. 12. Application of integrated sensor package to the pantograph: (a) 3D package designs, (b) sensor package installed on the joint of a pantograph, and (c) illustration of the lifted pantograph.

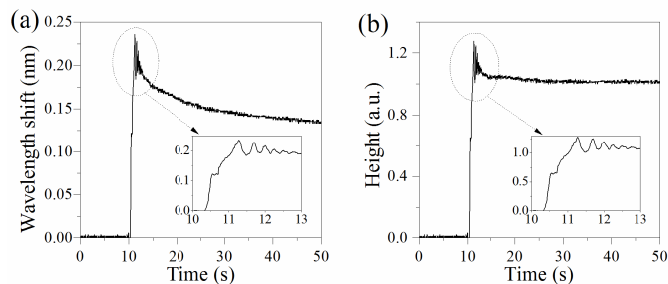


Fig. 13. Smart pantograph for height monitoring: (a) original data of Bragg wavelength shift collected when the pantograph hits the overhead wire and (b) reconstructed curve of the height of the pantograph.

B. Height Measurement

Fig. 13 shows the results of a height monitoring experiment by using this ‘smart pantograph’ so designed, applying the curve reconstruction method discussed. When a compressor is used to lift the arm, a measurement made using the sensor shows that the Bragg wavelength had shifted. However, in practice, while maintaining the height of the pantograph, the Bragg wavelength was seen continuously to shift (and approach its original wavelength) because of the viscoelasticity of the plastic material, as illustrated in Fig. 13(a). Fig. 13(b) shows the normalized actual, correct height data can be obtained using the reconstructed algorithm. The inset in this figure shows the detail of the impact, over the time period from 10 to 13 s, corresponding to when the pantograph hits the wire. This result obtained validates the supposition that the height can be more precisely monitored after the effect of the viscoelasticity in the smart

sensor has been eliminated, and the detail of the ‘hits’ of the pantograph on the wire can still be precisely represented.

7. Conclusion

In this research, various methods were used to identify the viscoelastic effect on FBG-based sensor systems. A data process method, based on deconvolution theory, has been proposed for eliminating the interfering effect, due to the presence of viscoelasticity, on the measurement made. An integrated 3D-printed dumbbell sensing specimen, comprising an FBG written into the fiber and the polymer was used as an example, examined in a uniaxial tensile test to validate the relevance of the viscoelastic effect and then provide a solution to allow the key measurement to be made. To illustrate this, a practical engineering application of a 3D-printed sensing package, used with the data process method described, was explored – in this case to monitor the height of a railway pantograph, allowing this to be done in the presence of electromagnetic interference.

The following conclusions on the design and validation experiment carried out can be drawn:

- 1) The polymer materials are viscoelastic, thus the measurement accuracy achievable from a POF, FBGs glued into a structure using adhesive, and polymer-based sensing package integrated with FBGs, can be affected by the material viscoelasticity.
- 2) A deconvolution-based algorithm to eliminate the viscoelastic effect has been put forward and used to demonstrate its efficacy through a uniaxial tensile test of a dumbbell specimen comprised of FBG sensors and polymers.
- 3) A 3D-printed package has been seen as a simple and inexpensive way to overcome the drawbacks of the use of conventional FBG sensors, enabling a large elongation test to be successfully carried out.
- 4) In an experimental validation using an important industrial example, the height of a railway pantograph can be measured effectively by using an integrated sensor, coupled to the data process method described.

Because the viscoelastic phenomenon is seen universally in a range of sensing packages, especially in the case when polymer materials are used in the sensors, the adhesives, and the 3D-printing packages, the solution discussed can have a positive impact on the sensing community in allowing sensors to be packaged effectively for field use, yet still achieving good measurement accuracy in practice. Furthermore, several shortcomings that are familiar from conventional optical fiber sensor packages, such as limited elongation, can be effectively improved by using the sort of customized polymer packages described. The benefits of these techniques can then be beneficial in various smart structure applications. And could be applied and validated in a wide range of industrial situations.

Funding Information. National Natural Science Foundation of China (No. 51605224); State Key Laboratory of Mechanics and Control of Mechanical Structures (No. 0516G02).

Acknowledgments. The authors would like to thank Brecknell Willis for helpful comments. Kenneth Grattan acknowledges the contribution from the George Daniels Educational Trust and both he and Tong Sun acknowledge the support from the Royal Academy of Engineering. Hongzhou Zhai is grateful to Nanjing University of Aeronautics and Astronautics for supporting the short-term visiting program.

References

1. A. D. Kersey, M. A. Davis, H. J. Patrick, M. LeBlanc, K. P. Koo, C. G. Askins, M. A. Putnam, E. J. Friebele, "Fiber Grating Sensors," *J. Light. Technol.* **15**(8), 1442–1463 (1997).
2. Q. Wu, F. Yu, Y. Okabe, and S. Kobayashi, "Application of a novel optical fiber sensor to detection of acoustic emissions by various damages in CFRP laminates," *Smart Mater. Struct.* **24**, 015011 (2015).
3. T. Grandal, S. Fraga, J. A. Vazquez, and A. Zornoza, "Technique for embedding fiber optics in metallic structures for smart material applications", in *Proceedings of the 8th European Workshop on Structural Health Monitoring (EWSHM, 2016)*, pp. 2100–2106.
4. Q. Li, G. Li, and G. Wang, "Effect of the plastic coating on strain measurement of concrete by fiber optic sensor," *Measurement* **34**, 215–227 (2003).
5. T. K. Gangopadhyay, M. Majumder, A. K. Chakraborty, A. K. Dikshit, D. K. Bhattacharya, "Fibre Bragg grating strain sensor and study of its packaging material for use in critical analysis on steel structure," *Sensors Actuators, A Phys.* **150**, 78–86 (2009).
6. G. Rajan, M. Ramakrishnan, Y. Semenova, E. Ambikairajah, G. Farrell, G. Peng, "Experimental study and analysis of a polymer fiber bragg grating embedded in a composite material," *J. Light. Technol.* **32**(9), 1726–1733 (2014).
7. L. Fang, T. Chen, R. Li, and S. Liu, "Application of Embedded Fiber Bragg Grating (FBG) Sensors in Monitoring Health to 3D Printing Structures," *IEEE Sens. J.* **16**(17), 6604–6610 (2016).
8. M. G. Zubel, K. Sugden, D. Saez-Rodriguez, K. Nielsen, and O. Bang, "3-D printed sensing patches with embedded polymer optical fibre Bragg gratings," *Proc. SPIE* 9916, 99162E (2016).
9. Z. F. Zhang, C. Zhang, X. M. Tao, G. F. Wang, G. D. Peng "Inscription of polymer optical fiber Bragg grating at 962 nm and its potential in strain sensing," *IEEE Photonics Technol. Lett.* **22**(21), 1562–1564 (2010).
10. J. Li, Z. Zhou, and J. Ou, "Interface transferring mechanism and error modification of embedded FBG strain sensor based on creep: Part I. linear viscoelasticity," *Proc. SPIE* 5765, 1061-1072 (2005).
11. M. C. J. Large, J. Moran, and L. Ye, "The role of viscoelastic properties in strain testing using microstructured polymer optical fibres (mPOF)," *Meas. Sci. Technol.* **20**, 034014 (2009).
12. M. Liang, N. Chen, X. Fang, and G. Wu, "Strain transferring mechanism analysis of the surface-bonded FBG sensor," *Appl. Opt.* **57**, 5837–5843 (2018).
13. Glass Transition Temperature, "Glass Transition Temperature Values of Several Plast," <https://omnexus.specialchem.com/polymer-properties/properties/glass-transition-temperature>.
14. J. M. Dealy and J. Wang, *Melt Rheology and its Applications in the Plastics Industry*, (Springer, 2013), Chap. 3.
15. Q. Wu, T. Ogasawara, N. Yoshikawa, and H. Zhai, "Modeling the viscoelasticity of polyetherimide," *J. Appl. Polym. Sci.*, 46102 (2018).
16. ISO 527-1, "Plastics-Determination of tensile properties-Part 1: General principles," <https://www.iso.org/standard/56045.html>
17. ISO 527-2, "Plastics-Determination of tensile properties-Part 2: Test conditions for moulding and extrusion plastics," <https://www.iso.org/standard/56046.html>
18. H. Wang and Z. Zhou, "Advances of strain transfer analysis of optical fibre sensors," *Pacific Sci. Rev.* **16**, 8–18 (2014).
19. D. Li, H. Li, L. Ren, and G. Song, "Strain transferring analysis of fiber Bragg grating sensors," *Opt. Eng.* **45**(2), 024402 (2006).
20. H. Li and G. Zhou, "Strain transfer analysis of embedded fiber Bragg grating sensor under nonaxial stress," *Opt. Eng.* **46**(5), 054402 (2007).
21. M. Lai, D. Karalekas, and J. Botsis, "On the effects of the lateral strains on the fiber Bragg grating response," *Sensors* **13**, 2631–2644 (2013).
22. K. Peters, "Polymer optical fiber sensors—a review," *Smart Mater. Struct.* **20**, 013002 (2011).